Study of the sputtered Cu atoms and Cu^+ ions in a hollow cathode glow discharge using a hybrid model

N. Baguer[a] and A. Bogaerts
Department of Chemistry, University of Antwerp, Universiteitsplein 1, B-2610 Wilrijk-Antwerp, Belgium

(Received 10 January 2005; accepted 22 June 2005; published online 10 August 2005)

The role of the Cu atoms sputtered from the cathode material in a cylindrical hollow cathode discharge (HCD) and the corresponding Cu^+ ions are studied with a self-consistent model based on the principle of Monte Carlo (MC) and fluid simulations. In order to obtain a more realistic view of the discharge processes, this model is coupled with other submodels, which describe the behavior of electrons, fast Ar atoms, Ar^+ ions, and Ar metastable atoms, also based on the principles of MC and fluid simulations. Typical results are, among others, the thermalization profile of the Cu atoms, the fast Cu atom, the thermal Cu atom and Cu^+ ion fluxes and densities, and the energy distribution of the Cu^+ ions. It was found that the contribution of the Ar^+ ions to the sputtering was the most significant, followed by the fast Ar atoms. At the cathode bottom, there was no net sputtered flux but a net amount of redeposition. Throughout the discharge volume, at all the conditions investigated, the largest concentration of Cu atoms was found in the lower half of the HCD, close to the bottom. Penning ionization was found the main ionization mechanism for the Cu atoms. The ionization degree of copper atoms was found to be in the same order as for the argon atoms (10^{-4}). © *2005 American Institute of Physics*. [DOI: 10.1063/1.2005381]

I. INTRODUCTION

When the ions and neutral gas atoms bombard the cathode surface of a glow discharge, different processes may occur: the atoms and ions can be reflected or implanted, can provoke structural rearrangements in the surface layers of the cathode material, can induce secondary-electron emission, and can also generate a series of collisions between the atoms of the cathode surface. This can lead to the ejection of some atoms of the target surface (i.e., so-called sputtering) or the cascade can go deep into the interior of the target, transferring the energy to lattice vibrations (heat).[1,2] When sputtering happens, the ejected particles are mostly single ground-state neutral atoms, but moving away from the cathode, they can react with the other species present in the discharge, and the sputtered atoms can become ionized.

Hollow cathode discharge (HCD) is extensively used in laser technologies,[3,4] spectroscopic analysis,[5–7] and plasma processing (ion etching, thin-film deposition, surface treatment).[8,9] Many of these applications are based on the sputtering of the cathode material by energetic ions and atoms. HCDs are a good medium to obtain high fluxes of energetic particles. The loss of energetic particles [to the anode(s) and to the walls] is considerably reduced due to its geometric configuration.[10,11] Hence, most of the energy of the fast particles is spent inside the discharge for the production of new electron-ion pairs, which allows lower operating voltages than in conventional planar cathode glow discharges. Consequently, HCDs give high rates of sputtering while maintaining the discharge voltage relatively low, which decreases the probabilities of overheating the cathode surface as well as the radiation damage of the substrate.

Due to the inhomogeneity of the discharge, the spatial distribution of the sputtered particles is not uniform. Hence, in order to improve the use of HCDs for the above-mentioned applications, it is important to study the fundamental aspects of sputtering, such as the spatial distribution of the sputtered particles, their transport and interaction with the other plasma species, as well as the best conditions for optimal sputtering.

Experimental studies on HCDs are based on atomic emission,[5,6,12] absorption,[13–15] fluorescence,[16] and mass spectrometry.[17] Theoretical works are mainly based on numerical simulations. By modeling the sputtering process in HCDs, the metal atom population is calculated based on the solution of the continuity and flux equations. In some works[18–21] the creation rate for the sputtered atoms is deduced from the total discharge current (to obtain a value for the impinging ion flux to the cathode) and from the applied potential (i.e., the average energy of the bombarding gas ions, needed to determine the sputtering yield, is taken in accordance with the cathode fall potential). This source term can also be given by the thermalization profile like, for example, in the work of Oliver and Finlayson,[22] where the initial flux of sputtered metal atoms was generated by a Monte Carlo (MC) model in combination with experimental data, and the thermalization profile was calculated based on the continuous slowing down approximation.[23] However, by tracking the sputtering in that way, the solution is not self-consistently calculated. Indeed, the energy distribution of the particles bombarding the cathode, which is the most important parameter for determining the sputtered flux, is not calculated in the model, but is deduced based on experimental parameters (discharge current and cathode fall potential). Hence, it is not possible to obtain the spatial dependence of the sputtered flux. A self-consistent calculation of the sput-

[a]Electronic mail: neyda.baguer@ua.ac.be

tered atom density can be carried out, for example, by calculating the energy distribution function of the energetic particles analytically[24] or by solving the Boltzman transport equation[25] and, subsequently, the Poisson equation together with the continuity equations in order to obtain the particle densities and the electric-field strength.

Another way of self-consistently calculating the sputtered atom density is given by the hybrid approach, based on a combination of MC and fluid models. With the MC approach[26,27] the microscopic nature of particles and their interaction can be considered explicitly. On the other hand, the fluid method[28,29] considers no individual particle but treats them as a continuum. The transport of each kind of particle is described by solving the continuity and flux equations. Moreover, in the case of charged particles the transport equations are coupled with the Poisson equation in order to obtain the electric-field strength. The source terms for the continuity equations in the fluid model are taken from the collision rates, which are calculated in the MC models, based on the energy-dependent cross sections, while the particle energy is calculated from the electric field. In that way not only the flux energy distribution of the particles bombarding the cathode can be calculated, but also the interaction of the sputtered atoms with the plasma species can be followed in a more realistic way. The hybrid approach was used to describe the plasma behavior, and the sputtered species in HCDs, for example, in Ref. 30 for a segmented HCD and in Ref. 31 for a longitudinal HCD, respectively. These models were concerned with modified HCD configurations, intended for laser applications, which operate at higher pressures and currents than conventional HCDs.[32]

In the present paper we will study, by means of a hybrid model, the processes responsible for the cathode sputtering, the transport of the sputtered atoms and the corresponding ions, as well as their interaction with the other species in a cylindrical (conventional) HCD. This approach will allow us to calculate in a self-consistent manner the electric field and the energy distribution functions of the energetic particles, which are not only crucial for the correct description of the electrical properties of the discharge but also for the description of the sputtering. Indeed, in this way, the energy and particle fluxes of the energetic particles bombarding the cathode, as well as the fluxes and densities of the sputtered atoms and corresponding ions, are calculated directly and self-consistently in the model. Hence, a better description of excitation and ionization processes of the sputtered atoms can be achieved, which is crucial for application purposes. For example, in analytical chemistry, where cathode sputtering is the way of sample atomization, it is important for atom absorption spectrometry to find the place where the concentration of sample (sputtered) atoms and ions is highest in order to improve the absorption signal. Moreover, for atom emission spectrometry, it is useful to improve the analyte spectral line emission intensity, and for mass spectrometric analysis, it is important to optimize the outgoing ion flux. Also in the metal vapor and metal-ion laser technologies, where the sputtered atoms and the corresponding ions constitute the active medium, it is useful to know their density distribution as well as the density distribution of the metastable atoms and ions from the carrier gas in order to optimize the lasing transitions and, therefore, to improve the laser construction.

II. DESCRIPTION OF THE MODELS

A. Assumptions of the model

The discharge gas was assumed to be argon at room temperature and uniformly distributed throughout the discharge, i.e., the thermal motion of the gas atoms is neglected. The other species considered in the model are singly charged positive argon and copper ions, metastable Ar atoms (Ar^m), fast and slow electrons, fast Ar atoms (Ar^f), and fast (Cu^f) and slow Cu atoms.

The Ar^f atoms are formed by elastic collisions of Ar^+ ions and Cu^+ ions with the background Ar gas, and they are assumed to have energies higher than 1 eV. The fact that we consider a fraction of the Ar atoms as fast particles does not contradict the assumption that the gas is uniformly distributed throughout the discharge, because the Ar^f density is four orders of magnitude lower than the density of the discharge gas.[33] Nevertheless, the Ar^f play a significant role in the sputtering process as will be shown later in the paper.

The Cu^f are the sputtered atoms from the cathode. The Cu atoms are emitted with an initial energy of several eV and they are considered as fast particles until they become thermalized, i.e., mainly due to elastic collisions with the background Ar gas.

The fast Ar^+ and fast Cu^+ ions are considered in the cathode dark space (CDS), where these ions gain energy from the electric field and they are described through a MC approach.

The electrons are split up in two groups:[34] the fast electrons, with high enough energy to cause inelastic collisions, and the slow electrons, which do not have enough energy. The energy threshold for considering electrons as fast particles was 4.6 eV, which corresponds to the ionization energy from the Ar^m levels.

The two metastable levels of Ar, $^3P_2$ and $^3P_0$, which lie at 11.55 and 11.72 eV above the ground state, respectively, have been combined into one collective level lying at 11.55 eV.[35] This assumption was made based on the fact that the $^3P_0$ level was considerably less populated than the $^3P_2$ level,[36,37] and for our purpose only the total metastable density is important.

In the following, we will emphasize on the description of the models for the Cu atoms and Cu^+ ions. The models developed for the other species (electrons, Ar^+ ions, Ar^f, and Ar^m) were explained in previous papers.[33,37,38]

B. Monte Carlo model for the sputtered Cu atoms

The cathode sputtering can be treated as a probability process in which every time that an energetic particle impinges the cathode, the ejection of the atoms will occur with a certain probability given by the energy and angle of incidence of the impinging particle, i.e., following the principle of particle-in-cell simulations. However, to accomplish it, a very long calculation time is required. Therefore, in the present model, we have opted to calculate the sputtered flux based on the Matsunami formula[39] for the sputtering yield

and the energy flux distribution of the particles bombarding the cathode. This approach is sufficiently accurate and much faster.

The sputtered flux (J^{Cu}) is calculated as the product of the sputter yields as a function of energy (E) (i.e., the number of atoms ejected per incident particle)[39] and the bombarding particle flux energy distributions (f_{cat}), integrated over the complete energy range:

$$J^{Cu} = -\int (Y^{Ar^+,Cu}(E)(f_{cat}^{Ar^+}(E) + f_{cat}^{Ar^{f+}}(E)) + Y^{Cu^+,Cu}(E) f_{cat}^{Cu^+}(E))dE, \quad (1)$$

where the negative sign indicates that the sputtered flux is in the opposite direction as the bombarding fluxes.

The spatial dependence of the sputtered flux was calculated based on an approximation of Eq. (1), where instead of the flux energy distribution, the particle flux at the cathode (at each grid point of the cathode, i) was used and the sputtering yield was calculated for the average energy (E_{ave}) at each i:

$$j_i^{Cu} = -(Y^{Ar^+,Cu}(E_{ave}^{Ar^+})_i j_{i_{cat}}^{Ar^+} + Y^{Ar^f,Cu}(E_{ave}^{Ar^f})_i j_{i_{cat}}^{Ar^f} + Y^{Cu^+,Cu}(E_{ave}^{Cu^+})_i j_{i_{cat}}^{Cu^+}). \quad (2)$$

Subsequently, the relative spatial distribution, $j_i^{Cu}/\Sigma_i j_i^{Cu}$, was factorized by the value of the total sputtered flux (J^{Cu}) calculated in Eq. (1).

The initial position of the Cu atoms, i.e., the position from where they are ejected from the cathode surface, was determined by the relative spatial distribution of the sputtered flux (see above) and by generation of random numbers (rn's). The Cu atoms are assumed to be ejected from the cathode following the Sigmund-Thompson distribution[40] from where the initial energy E and the axial (ϑ) and azimuthal (φ) angles of the initial velocity were calculated as $E=U/(rn^{-0.5}-1)$, $\theta=0.5\arccos(1-2rn)$ and $\varphi=2\pi rn$, respectively. U is the surface binding energy of the cathode material, which is taken equal to the heat of sublimation. Based on the fact that the maximum energy which a colliding particle can transfer in a collision corresponds to the energy transfer in a head-on elastic collision, it was assumed in the model that the maximum initial Cu atom energy (E_{max}^{Cu}) will be equal or less than $[4m^{Cu}m^{Ar}/(m^{Cu}+m^{Ar})^2]E_{ave}^{Ar^+}$, where $E_{ave}^{Ar^+}$ is the average Ar^+ ion energy at the point of emission. Due to elastic collisions, this initial energy is transferred very effectively to the background gas. In Ref. 23 it was shown that the thermalization of the sputtered atoms occurs on a very short time scale and can be considered to be finished when the diffusion starts, hence both processes can be modeled separately. This MC submodel handles the evolution of the sputtered Cu atoms toward the thermalization, while in the fluid submodel for Cu^+ ions and Cu atoms (see below) the transport by diffusion of the Cu atoms is described.

During each time step, the trajectory of the Cu atoms is calculated with Newton's laws: $\mathbf{r}=\mathbf{r}_0+\mathbf{v}\Delta t$, where Δt is the time interval and $\mathbf{r}_0,\mathbf{r}$ are the position vectors before and after Δt, respectively, and $\mathbf{v}$ is the velocity vector. We considered here that the slowdown of the sputtered Cu atoms is only due to elastic collisions with background Ar atoms, because this process has the highest cross section and the density of the other species present in the discharge is at least four orders of magnitude lower than the background Ar atom density.[33,38] Due to a lack of information about experimental Cu elastic cross sections with Ar atoms [$\sigma(E_0)$], the value of $\sigma(E_0)$ was obtained from Lindhard's differential scattering cross section,[41] $\sigma(E_0,T)$, after integration over all possible values of energy transfer T from a projectile of energy E_0 to an atom at rest. The interatomic interaction potential was taken in the form proposed by Sielanko,[42] i.e., a power-law potential that approximates the Molier potential by taking the inverse power potential parameter as a function of the impinging energy and impact parameter.

The probability of elastic collisions during the time step Δt is calculated by $P=1-\exp[-\Delta s n^{Ar}\sigma(E_0)]$, where Δs is the distance traveled by the Cu atoms with energy E_0 during the interval Δt and n^{Ar} is the density of the background Ar atoms. Subsequently, P is compared to a rn in order to determine if a collision takes place. After each collision, the new energy and velocity direction are calculated: the axial scattering angle χ was calculated from the Sielanko formula[42] and the energy after the collision, E, as $E=E_0-T$, where $T=E_0[4m^{Cu}m^{Ar}/(m^{Cu}+m^{Ar})^2]\sin^2\chi/2$. The conversion of the scattering angle into the laboratory frame of reference was done by the ordinary transformation of the coordinate frame of reference.[43]

This procedure of following the atoms with Newton's laws and describing their collisions with cross sections and rn's is repeated until the Cu atoms collide at the cathode walls or at the anode, where they can be absorbed or reflected, or until their energy drops below 0.03 eV, i.e., when they can be considered as thermalized Cu atoms.

By following in this way a large number of sputtered atoms, the thermalization profile (i.e., the spatial distribution of thermalized Cu atoms) is calculated, and this yields the initial distribution for further diffusion transport of the thermalized Cu atoms.

C. Fluid model for the Cu^+ ions and Cu atoms

This model describes the behavior of the thermalized Cu atoms and the corresponding Cu^+ ions. The ionization processes considered for the Cu atoms are electron impact ionization, Penning ionization by Ar^m, and asymmetric charge-transfer collision (ACT) with Ar^+ ions. The transport of the thermalized Cu atoms is diffusion dominated, while the Cu^+ ion transport is determined by drift and diffusion.

The following continuity and flux equations describe the behavior of the Cu atoms and Cu^+ ions:

$$\frac{\partial n^{Cu}}{\partial t} + \nabla \cdot \mathbf{j}^{Cu} = S_{prod}^{Cu} - S_{loss}^{Cu}, \quad (3)$$

$$\mathbf{j}^{Cu} = -D^{Cu}\nabla n^{Cu}, \quad (4)$$

$$\frac{\partial n^{Cu^+}}{\partial t} + \nabla \cdot \mathbf{j}^{Cu^+} = S_{prod}^{Cu^+}, \quad (5)$$

$$\mathbf{j}^{Cu^+} = -n^{Cu^+}\mu^{Cu^+}\nabla V - D^{Cu^+}\nabla n^{Cu^+}, \quad (6)$$

where,

$$S_{prod}^{Cu} = J^{Cu}F_t,$$

$$S_{loss}^{Cu} = S_{prod}^{Cu^+} = S_{e,ion,Cu} + k_{ACT}n^{Cu}n^{Ar^+} + k_{Pen}n^{Cu}n^{Ar^m}$$

n^{Ar^+} and n^{Ar^m} are the Ar^+ ion and Ar metastable atom densities, respectively. n^{Cu}, n^{Cu^+}, $\mathbf{j}^{Cu}$, $\mathbf{j}^{Cu^+}$, D^{Cu}, and D^{Cu^+} are the densities, fluxes, and diffusion coefficients of Cu and Cu^+, respectively. μ^{Cu^+} is the mobility of Cu^+ ions in Ar gas. The values of these coefficients were adopted from Ref. 44: $\mu^{Cu^+}=1837.4\ cm^2\ s^{-1}\ V^{-1}$, $D^{Cu^+}=D^{Cu}=144.6\ cm^2\ s^{-1}$ at 1 Torr. The production of Cu atoms (S_{prod}^{Cu}) is given by the normalized thermalization profile of the Cu atoms (F_t) factorized by the total sputtered flux of Cu atoms: $J^{Cu}=J_r^{Cu}+J_z^{Cu}$, where J_r^{Cu}, J_z^{Cu}, and F_t are calculated in the MC model for fast Cu atoms (see Sec. II B) and the subscripts r and z denote the sputtering from the the cylinder sidewalls and cathode bottom, respectively. The term S_{loss}^{Cu} represents the loss of Cu atoms due to the ionization processes considered. Hence, this term also gives the creation rate of the Cu^+ ions. $S_{e,ion,Cu}$ is the electron-impact ionization rate of Cu, calculated in the MC model for the fast electrons.[37] The second and third terms of S_{loss}^{Cu} stand for the ionization rate of Cu atoms by ACT with Ar^+ ions and by Penning ionization with Ar^m, respectively. The rate coefficient for ACT with Ar^+ ions (k_{ACT}) and for Penning ionization (k_{Pen}) were taken equal to be 2×10^{-10} and $2.6\times10^{-10}\ cm^3\ s^{-1}$, respectively.[44]

The continuity equations of Cu^+ ions and Cu atoms are coupled through $S_{loss}^{Cu}=S_{prod}^{Cu^+}$. Both equations are discretized and solved with the extended Thomas algorithm for a pentadiagonal matrix.[45] The boundary conditions for this system were determined by the sticking coefficients of copper atoms and ions. For the Cu atoms, a sticking coefficient of 0.5 was assumed, which means that at the walls the Cu atoms will be reflected or absorbed in the same proportion. This value was assumed based on the experimental evidence that the sticking coefficient for the sputtered atoms should be less than 1 (Ref. 14) and on the comparison between measured and calculated sputtered densities presented in Ref. 46. As boundary conditions for the Cu^+ ions, a complete recombination at the walls (anode and cathode) is assumed, i.e., a sticking coefficient equal to 1, $n^{Cu^+}=0$.

D. Monte Carlo model for the fast Cu^+ ions

The MC simulation for the Cu^+ ions is carried out in a similar way as for the Ar^+ ions,[33] i.e., they are followed only as fast particles inside the CDS. The Cu^+ ions start at the CDS-negative glow (NG) boundary or within the CDS with an assumed initial energy of 0.05 eV and a velocity direction parallel to the electric field. For the ions starting at the CDS-NG interface the initial position is determined from the radial and axial Cu^+ ion flux diffusing from the NG to the CDS, as calculated in the Cu, Cu^+ fluid model (see Sec. II C). As a result of the electron-impact ionization, Penning ionization, and ACT collisions, some new ions are created inside the CDS. The initial position of these ions is obtained from the corresponding ionization rates (calculated in the fast electron MC model and in the Cu, Cu^+ fluid model, respectively). During each time step the trajectory of the ions is calculated with Newton's laws:

$$\mathbf{r} = \mathbf{r}_0 + \mathbf{v}_0\Delta t + \frac{q\mathbf{E_f}}{2m^{Cu}}\Delta t^2, \quad \mathbf{v} = \mathbf{v}_0 + \frac{q\mathbf{E_f}}{m^{Cu}}\Delta t, \quad (7)$$

where $\mathbf{E_f}$ is the electric field, m^{Cu} is the Cu atomic mass, q is the particle charge, Δt is the time interval, and $\mathbf{r}_0$, $\mathbf{v}_0$ and $\mathbf{r}$, $\mathbf{v}$ are the position and velocity vectors before and after Δt respectively. The only collision process considered for the fast Cu^+ ions was the elastic collision with the background Ar atoms. In Lindhard's differential scattering cross section, no difference was made for neutral or charged projectiles. Therefore, we have applied the same analytical formula for the calculation of the Cu^+ ion elastic cross section as for the fast Cu atom cross section. Hence, for determining the occurrence of collisions and also the energy and velocity direction after collisions, the same assumptions as for the Cu^f were made. This procedure is repeated until the Cu^+ ions collide at the cathode walls or the anode, where they are neutralized and disappear from the calculations. As a result of Cu^+ ion elastic collisions with the background Ar atoms, Ar^f can be formed. These Ar^f are followed in the MC model for Ar^+ ions and Ar^f in the same way as is described in Ref. 33

E. Coupling of the submodels

The various submodels are coupled to each other due to the interactions between the different plasma species. Hence, the output of one model is used as input in the other models and the models are run iteratively, until convergence is reached. The latter is determined by the difference in the total current to the anode in two successive iterations, which should be below 0.05%. Typically, three to four iterations were carried out before convergence was reached.

III. RESULTS

The models were applied to a HCD consisting of a cylindrical cathode closed at one end and a disc anode at the other end separated by 0.2 cm (see Fig. 1 of Ref. 38). The discharge conditions assumed in the model were taken from experiment, i.e., the gas pressure was varied from 0.3 to 1.0 Torr, the discharge current ranged from 1 to 10 mA, and a discharge voltage between 240 and 300 V was applied to the cathode, whereas the anode was grounded. The gas temperature was assumed to be 300 K.

A. Fluxes of bombarding species at the cathode

The sputtered flux from the cathode [Eq. (1)] is determined by the flux energy distribution of the heavy particles bombarding the cathode [i.e., atoms and ions from the discharge gas, as well as ions from the cathode metal (so-called self-sputtering)], multiplied with the sputtering yield. The relative importance of Ar^+ ions, Ar^f, and Cu^+ ions for the sputtering process can be inferred from Fig. 1, where the flux energy distributions at the hollow cathode surface are plotted

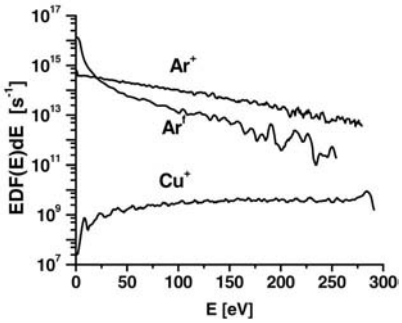

FIG. 1. Calculated flux energy distribution of the Ar^+ ions, Ar^f, and Cu^+ ions bombarding the cathode surface at 0.3 Torr and 9 mA.

for a discharge current of 9 mA and a pressure of 0.3 Torr, which is a representative example for all the conditions investigated. The Ar^f have a dominant role, but only at low energies, because their energy distribution decreases rapidly with increasing energy. The same is true, but less pronounced for the Ar^+ ions. The Cu^+ ion energy distribution function shows the opposite behavior, because it increases with rising energy. Nevertheless, the Cu^+ ion flux is always several orders of magnitude lower than the Ar^+ ion and Ar^f fluxes. Hence, in the concerned energy range, the highest flux at the cathode corresponds to the Ar^+ ions. Keeping in mind that there is a threshold energy for the sputtering to occur,[39] and that the sputtering yield is an increasing function of the bombarding energy up to energies of 1000 eV,[47] the sputtered flux will be little for low bombarding energies. Integrated over the total energy range the contribution of the Ar^+ ions to the sputtering was found to be the most significant, followed by the Ar^f. For example, at the condition under study, the Ar^+ ions and Ar^f contribute about 85% and 15% to the total amount of sputtering, respectively. The role of self-sputtering was found to be negligible (less than 0.1%).

The relative contribution of the Ar^f rises slightly with decreasing current at low pressures. Indeed, when the discharge current drops, the CDS length increases, hence the Ar^+ ion elastic collision rate inside the CDS increases, and consequently, the ratio of Ar^f flux to Ar^+ ion flux increases as well.

As the pressure rises, the situation changes. At low currents, the sputtering is almost completely caused by the Ar^+ ions, due to the low energy of the fast atoms. Indeed, with increasing pressure, the Ar^+ ion elastic collision rate increases, and consequently, the amount of Ar^f increases, as before. However, the discharge voltage decreases as well (at constant current), hence the mean energy of the Ar^+ ions drops, and therefore, also the energy transferred to the Ar atoms. Moreover, the fast-atom energy relaxation length (determined by the elastic collision cross section) decreases and becomes smaller than the CDS length. Hence, the energy of the fast atoms, when they strike the cathode, drops below the sputtering threshold.

It is interesting to notice that, while the Ar^+ ion and Ar^f energy distributions peak at low energies, the Cu^+ ion energy distribution peaks at the maximum attainable energy, i.e., at the energy corresponding to the cathode fall potential. This is so, because the energy relaxation length of the Cu^+ ions

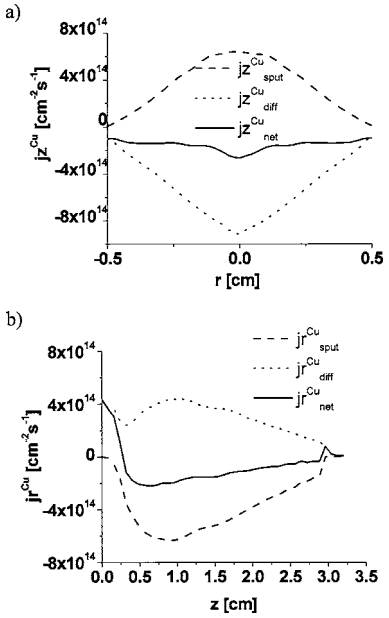

FIG. 2. Calculated ejected (j^{Cu}_{sput}), back diffusion (j^{Cu}_{diff}), and net sputtered (j^{Cu}_{net}) Cu-atom axial (a) and radial (b) fluxes at the cathode bottom and sidewalls, respectively, at 0.3 Torr and 9 mA.

(λ^{Cu^+}) is similar to the CDS length (d), while the energy relaxation length of the Ar^+ ions was found to be about six-times lower than d. For example, at 0.3 Torr and 9 mA, our calculations predict $d=0.18$ cm and $\lambda^{Cu^+}=0.15$ cm, while $\lambda^{Ar^+}=0.03$ cm. Moreover, due to the difference in mass between the Cu^+ and Ar^+ ions, the maximum energy transfer of Cu^+ ions to the discharge gas atoms will be less than for the Ar^+ ions. Hence, the Cu^+ ions traverse the CDS without many collisions with the gas atoms, while the collision frequency of the Ar^+ ions is higher and the energy transfer to the discharge gas more effective. Experimentally, this was also suggested by Hang and Harrison,[48] based on metal ion measured intensity profiles in glow discharges (GDs), and it corresponds also to findings by experimental and modeling work in planar GDs.[44,49]

B. Flux of sputtered atoms

The net flux of sputtered Cu atoms at the cathode consists of two contributions, one due to the ejected (sputtered) energetic atoms and another due to the transport by diffusion of the thermalized Cu atoms back to the cathode. In Fig. 2 the sputtered (ejected) flux, the back-diffusion flux, and the net sputtered Cu-atom flux at the cathode are plotted at 0.3 Torr and 9 mA as a representative example for all the conditions investigated.

At the cathode bottom, [Fig. 2(a)] the ejected flux is very low at the border ($r=0.5$ cm) and increases toward the center, where it stays almost constant. The flux due to back diffusion of the thermalized Cu atoms shows a sharp maximum at the center, decreasing very rapidly with the radial distance. The diffusion flux is always directed toward the cathode (i.e., back diffusion), as the density of thermalized atoms decreases in that direction, which is likely expected because of the relatively high energy (between 5 and

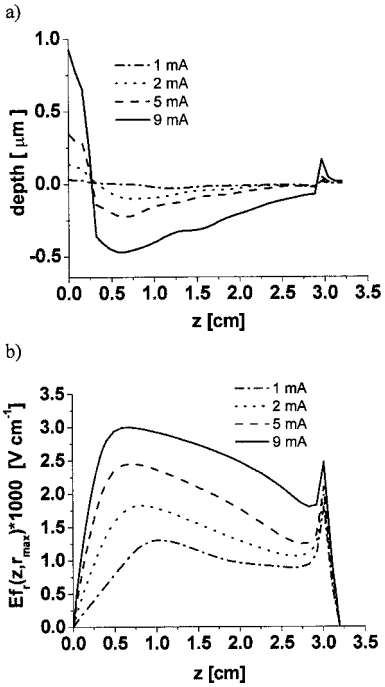

FIG. 3. Calculated depth profile at the cathode sidewalls after sputtering for 5 h (a), compared to the electric-field distribution at the sidewalls (b), at 0.3 Torr and at four currents.

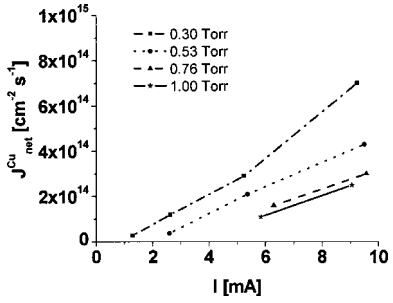

FIG. 4. Calculated net sputtered Cu-atom flux, integrated over the complete cathode surface, as a function of electrical current and at four different pressures.

15 eV)[50] of the atoms when sputtered from the cathode. Over the entire bottom surface, the back-diffusion flux predominates over the ejected flux. This results in a net flux of atoms redepositing at the cathode bottom ($jz_{\text{net}}^{\text{Cu}}$ is negative).

At the cathode sidewalls [Fig. 2(b)], the ejected Cu atom flux is very low at the "cathode corner" ($z=0$); it reaches a maximum at about 0.7 cm from the cathode bottom (i.e., in the first half of the cylinder) and then it decreases toward the anode. Note that a negative flux now indicates a flux away from the cathode surface and this is opposite from the axial direction (sputtering from the cathode bottom). The back-diffusion flux predominates over the ejected flux only at the region close to the bottom and at the open end of the cathode, where only the diffusion flux is present. Hence, there is a net sputtering from the cathode sidewalls ($jr_{\text{net}}^{\text{Cu}}$ is negative), except near the open end and especially near the cathode bottom, where there is significant redeposition ($jr_{\text{net}}^{\text{Cu}}$ is greatly positive).

This spatial behavior of the sputtered flux is common for all the discharge conditions investigated here: Along the bottom and sidewalls, the profile of the Cu atom fluxes (ejected, back diffusion, and net flux) is rather nonuniform. At the cathode bottom, there is a net flux of redeposition instead of sputtering. At the cathode sidewalls, the various fluxes are larger near the closed end of the hollow cathode. This is a direct consequence of the strong axial and radial electric field here, whereas in the rest of the CDS belonging to the cathode sidewalls, only the radial component of the electric field is strong (except at the open end). From the comparison of Figs. 3(a) and 3(b) we can indeed see that the cathode depth profile [Fig. 3(a)] due to the net sputtered flux at the cathode sidewalls reflects the spatial distribution of the electric-field strength at the cathode sidewalls. A weak radial electric field corresponds to a large amount of redeposition because of the small bombarding flux.

Our calculated Cu-atom depth profiles are consistent with the experimental observations of cut hollow cathodes, which show that the deeper crater is found in the first half of the HCD, i.e., that part of the HCD near the bottom (see, for example, Figs. 9 and 14 from Ref. 5 and Fig. 6 from Ref. 22), and that the cathode bottom after sputtering is thicker than before.

Integrated over the entire cathode surface (i.e., bottom and sidewalls), the net sputtered Cu-atom flux corresponds to about 20% of the total ejected flux at 0.3 Torr, due to the large amount of redeposition. It should be mentioned that the net sputtered flux from the cathode sidewalls represents 23% of the total ejected flux. This means that a certain fraction of the atoms ejected from the sidewalls redeposits at the cathode bottom. This ratio of about 20% was found the same for all values of the discharge current. Indeed, with decreasing current (at constant pressure), the net sputtered Cu-atom flux drops [see Figs. 3(a) and 4], because a decrease in current means a lower discharge voltage (at constant pressure) and lower particle fluxes, hence a drop in the flux energy distribution. However, the ratio of the net sputtered flux to the ejected flux stays nearly constant.

With increasing pressure, when the current is held constant, the net ejected flux of Cu atoms decreases (see Fig. 4), but the ratio of the net sputtered flux to the total ejected flux rises slightly. For example, at 1 Torr, the net sputtered flux represents about 26% of the ejected flux, while at 0.3 Torr it was found to be around 20%. This can be explained as follows: when the pressure increases at constant current, a lower voltage is needed to sustain the discharge, implying a shift of the flux energy distribution to lower energies, hence less sputtering, but at the same time, due to the increase in pressure, the diffusion drops, hence the back diffusion is slightly reduced.

C. Density of the Cu atoms

The ejected Cu atoms transfer most of their initial energy (typically 5–15 eV) very efficiently to the background discharge gas and, consequently, the majority of the sputtered atoms become thermalized already after a few collisions. This is clear from Fig. 5(a), which shows that the nonthermalized Cu-atom density profile has a maximum adjacent to

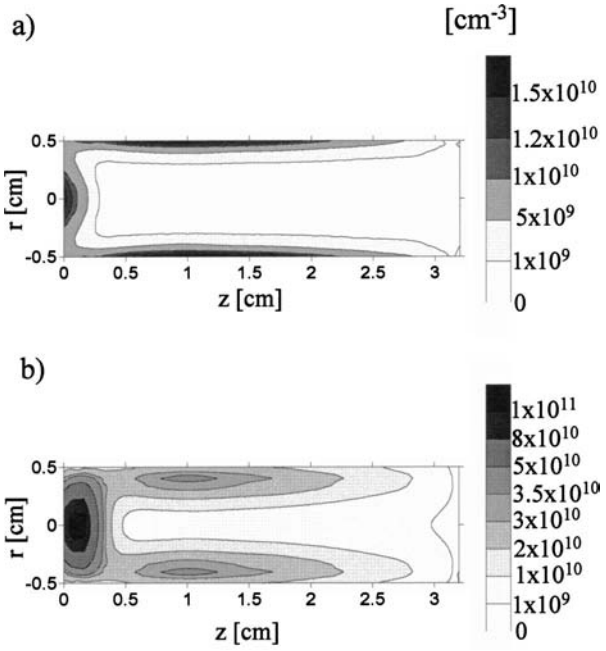

FIG. 5. Calculated two-dimensional density profiles of the nonthermalized (a) and thermalized (b) Cu atoms at 9 mA and 0.3 Torr.

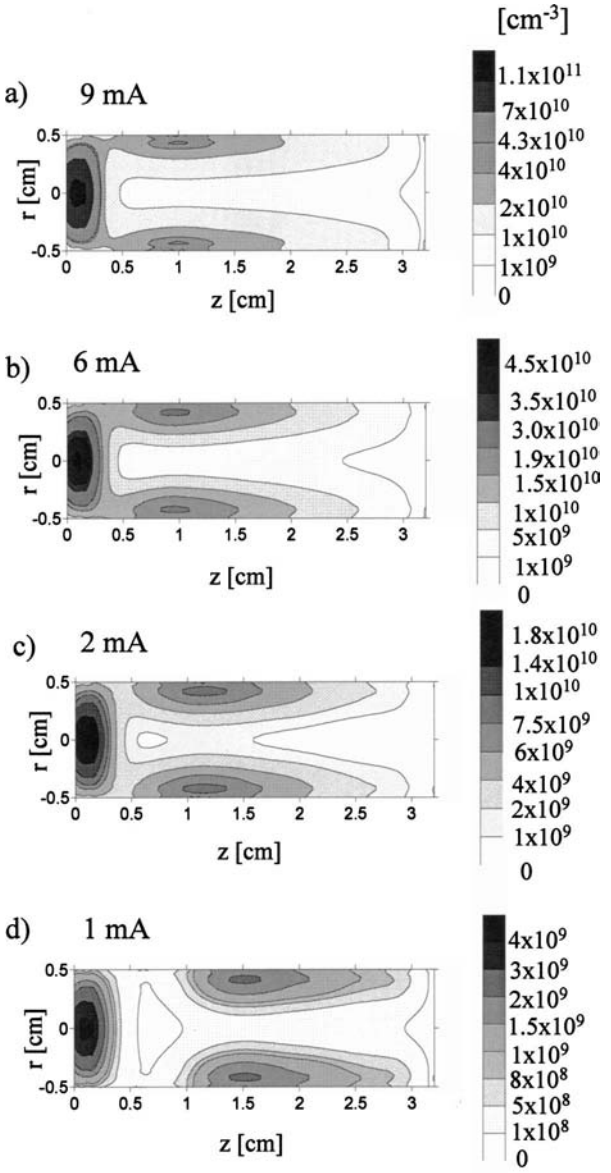

FIG. 6. Calculated two-dimensional profiles of the Cu-atom density at 0.3 Torr and four different currents: 9 (a), 6 (b), 2 (c) and 1 mA (d).

the cathode walls and becomes negligible after 1–2 mm from the cathode surface. Also the thermalized Cu-atom density profile [Fig. 5(b)] exhibits a maximum near the cathode walls, i.e., at about 1.2 mm for a discharge at 0.3 Torr and 9 mA. The total Cu-atom population is given by the sum of both groups: the nonthermalized and the thermalized Cu atoms. It should be noted that the density of the nonthermalized Cu atoms is much lower than that of the thermalized atoms: even at its maximum, it is still one order of magnitude lower, and throughout the discharge volume, their density is negligible compared to the thermalized Cu-atom density. Hence, the profile of the total Cu-atom density resembles closely the corresponding thermalized Cu-atom density profile, as can be seen from Fig. 6(a), which shows the total Cu-atom density profile at 9 mA and 0.3 Torr.

Figure 6 illustrates the total Cu-atom two-dimensional density profiles at 0.3 Torr and four different currents, and Fig. 7 shows the density profiles at 9 mA and four different pressures. In general, the total Cu-atom density peaks at the cell axis, close to the bottom surface. A second maximum is found between 0.5 and 1.5 cm from the cathode bottom, very close to the cathode sidewalls. Around the cylinder axis, away from the cathode bottom and sidewalls, the Cu-atom density is very low. At all the conditions investigated, the largest concentration of Cu atoms was always found in the lower half of the HCD, where the bombarding fluxes of energetic Ar^+ ions and atoms were at maximum (see above).

As it appears from Fig. 6, the Cu population decreases with decreasing discharge current at constant pressure, because the sputtered flux drops. At 0.3 Torr and all currents investigated, the maximum density is always reached at around 1 mm from the cathode surface, both from the cathode bottom and the sidewalls. Due to the increase of the CDS length at lower currents, the maximum of the Cu-atom density at the cathode sidewalls shifts in the direction of increasing z, from $z=1$ cm at 9 mA to $z=1.5$ cm at 1 mA. At 1 mA, a region of very low density appears at a distance of 0.6 cm from the cathode bottom, as if two independent zones of sputtering exist in the discharge, one due to the cathode bottom and another due to the cathode sidewalls.

It is clear from Fig. 7 that with increasing pressure, the Cu-atom population decreases and its maximum near the cathode bottom is found somewhat closer to the cathode surface, i.e., at 1, 0.7, 0.5, and 0.3 mm from the cathode bottom for 0.3, 0.53, 0.76, and 1 Torr, respectively. The reason is that the thermalization happens faster due to the decrease of the Cu mean free path.

Also, with increasing pressure, the first maximum near the cathode bottom drops, but the second maximum near the cathode sidewalls increases. For example, at 0.3 Torr [Fig. 7(a)] the maximum Cu-atom density, in front of the cathode bottom, is 2.5 times higher than the second peak at the cathode sidewalls. At 0.76 Torr, [Fig. 7(c)] both density peaks,

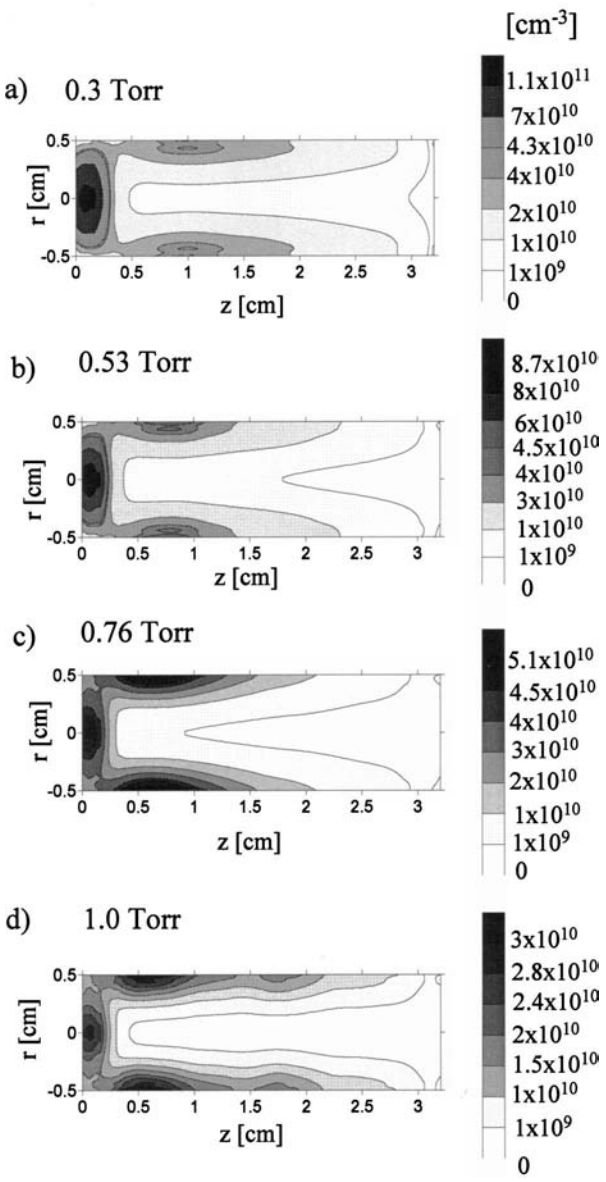

FIG. 7. Calculated two-dimensional profiles of the Cu-atom density at 9 mA and four different pressures: 0.3 (a), 0.53 (b), 0.76 (c), and 1.0 Torr (d).

near the cathode bottom and the sidewalls, have similar values, around 5×10^{10} cm^3. At still higher pressures [1 Torr, Fig. 7(d)] the maximum population of Cu atoms is found in front of the cathode sidewalls. This is probably the consequence of the lower diffusion with increasing pressure. At 1 Torr, the ejected (sputtered) Cu-atom flux from the cathode bottom represents 8% of the total ejected flux, integrated over the entire cathode surface, which corresponds exactly to the ratio of the cathode bottom area to the total area of the cathode cylinder. At 0.3 Torr, the ejected flux from the bottom represents only 2% of the total ejected flux. Moreover, at the cathode bottom, there is no net sputtered flux, but a net redeposition flux. Hence, the shift in the position of the Cu-atom maximum density from near the cathode bottom to near the cathode sidewalls when the pressure increases cannot be a consequence of the lower sputtering from the cathode bottom, because the latter, in fact, increases. For this reason, we think it is due to lower diffusion.

Moreover, at higher pressures, the drop in the density in the axial direction, as well as in the radial direction, is much more pronounced. This results in a significant dip at the cylinder axis, and in much lower Cu density values near the open end of the cylinder. For example, at 9 mA and 0.3 Torr the calculated Cu density at the cylinder axis, at $z=3$ cm, is approximately 10^9 cm^{-3}, while at 1 Torr it has dropped to 5×10^7 cm^{-3}, at $z=3$ cm.

It is interesting to notice that, at a pressure of 1 Torr, a third (small) peak appears near the cathode sidewalls at $z=1.8$ cm [see Fig. 7(d)], indicating that regions of higher metal density alternate with regions of lower density. In our opinion, the main reason for this spatial dependence of the Cu-atom density is the nonuniform distribution of the ion velocity at the cathode sidewalls, which is ultimately determined by the spatial distribution of the electric field. It should be pointed out that regions with well-defined different microstructure along the hollow cathode surface, as well as the formation of consecutive hollow spheres along the cathode sidewalls, have also been observed experimentally.[5,22,51]

D. Ionization processes of Cu atoms

The ionization mechanisms for Cu atoms included in the model are Penning ionization by Ar^m, ACT by Ar$^+$ ions, and (fast) electron-impact ionization. The electron-impact ionization rate was calculated directly in the MC model for the fast electrons through the energy-dependent cross section, while the ionization rates for Penning ionization and ACT collisions were calculated through the corresponding collision rate coefficients and the calculated Ar^m and Ar$^+$ ion densities, respectively. The rate coefficients of ACT and Penning ionization are in the same order of magnitude, hence, the difference in the corresponding collision rates is mainly given by the Ar^m and Ar$^+$ ion density distributions throughout the discharge. Therefore, in order to calculate accurate values for these rates, realistic Ar$^+$ ion and Ar^m densities are needed.

The Ar$^+$ ion density can be considered to be more or less correctly calculated in our model, as a very good agreement between calculated and measured current-voltage and spectrometric properties of the discharge was obtained (see Ref. 38 for more details).

Concerning the Ar^m density, in the present work, we have extrapolated the suggestion made in Ref. 37 for the production of Ar metastable atom density at 1 Torr to the other pressures, 0.53 and 0.76 Torr. Indeed, if we assume that at 1 Torr, the production of the collective Ar metastable level ($^3P_2$ and $^3P_0$ levels) by fast electrons, fast Ar$^+$ ions, and Ar^f is only due to direct excitation from the ground state, while at 0.3 Torr, it arises from contributions of direct excitation from the ground state as well as from cascading of the higher-lying states, then it seems straightforward to use some intermediate production rate for the metastable population at 0.53 and 0.76 Torr. In practice, this corresponds to reducing the total production rate by some factor, i.e., by 20% at 0.53 Torr and by 40% at 0.76 Torr. The resulting calculated densities were then in good agreement with the experimental values (see Ref. 37 for more details) and are used here to

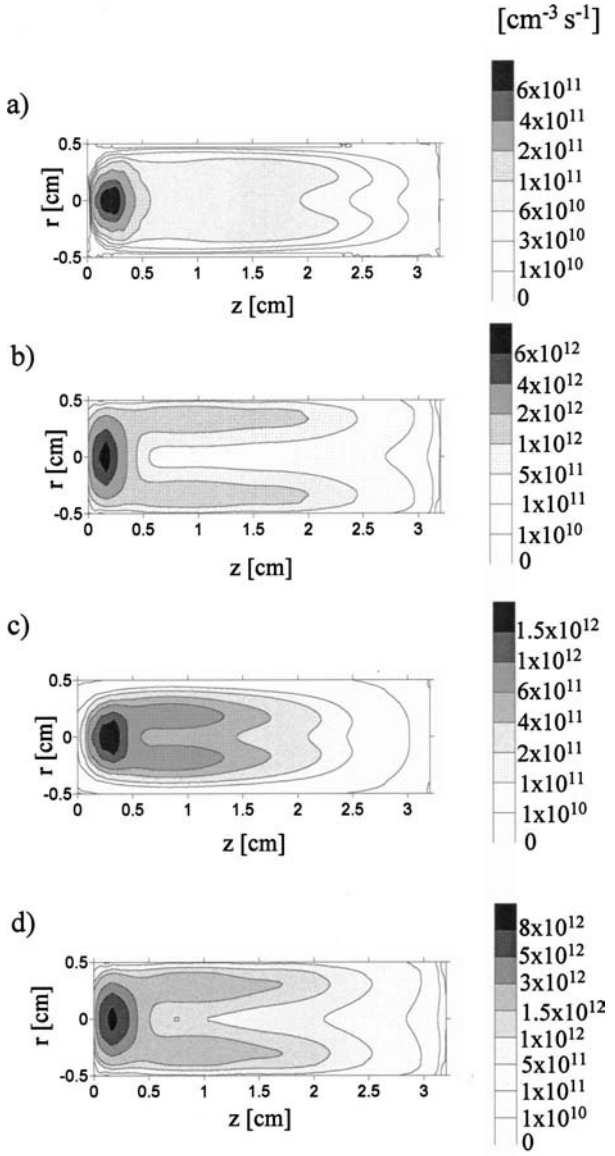

FIG. 8. Calculated two-dimensional collision rates of Cu atoms due to electron-impact ionization (a), Penning ionization (b), Ar^+ ion ACT collision (c), and total Cu ionization rate (d) at a pressure of 0.3 Torr and a current of 9 mA.

calculate the Penning ionization rate. Hence, we expect that the Penning ionization rate in our model yields also realistic values.

To illustrate the relative importance of the different ionization mechanisms throughout the discharge, the two-dimensional rate profiles of electron-impact ionization, Ar^+ ion ACT, and Penning ionization are presented in Fig. 8 for a discharge at 9 mA and 0.3 Torr.

The maximum of all the ionization rates was found around the cylinder axis and at few millimeters from the cathode bottom. Throughout the rest of the discharge, the spatial distribution of the ionization rates is somewhat different. The electron-impact ionization rate [Fig. 8(a)] is low near the cathode sidewalls and increases towards the NG, since the electrons are accelerated away from the cathode and reach their maximum energy at the end of the CDS. Hence, in spite of the fact that the Cu-atom density is high near the cathode surface, the electron-impact ionization rate is low here, since there are not enough energetic electrons. In the NG, the electron-impact ionization rate of the Cu atoms is more or less uniformly distributed. This is a consequence of the oscillatory movement of the electrons between the two opposite CDS regions and the fact that the Cu ionization threshold (i.e., 7.7 eV) is low compared to the maximum achievable electron energy, so that in the entire NG, there are enough electrons with sufficient energy for Cu ionization.

In the CDS, Penning ionization is the main ionization mechanism for the Cu atoms, as the density of the Ar^m is one order of magnitude higher than the Ar^+ ion density in this region. The Penning ionization rate peaks at the CDS-NG interface [see Fig. 8(b)]. Throughout the NG, Penning ionization is still the most important ionization mechanism, but ACT is only slightly less important. This is likely expected since the densities of the Ar^+ ions and Ar^m are similar in value and both densities peak at the discharge axis. Compared to the spatial profile of the Penning ionization rate, the maximum of the ACT profile is shifted toward the cylinder axis and is also more concentrated on the first half of the HCD [see Fig. 8(c)]. This is the result of the Ar^+ ion density profile, which exhibits a similar behavior,[38] while the Ar^m are more uniformly distributed in the axial direction.[37]

Integrated over the entire discharge volume, Penning ionization was calculated to be the dominant ionization mechanism of the Cu atoms, for all the conditions investigated, followed by ACT and electron-impact ionization. For example, at 9 mA and 0.3 Torr, the relative contribution of Penning ionization, ACT, and electron-impact ionization amount to 78%, 18%, and 4%, respectively. With decreasing current, at constant pressure, the role of Penning ionization still increases, as the densities of the Ar^+ ions and electrons decrease much faster with current than the Ar^m density. For the lower currents investigated (1 and 2 mA) at 0.3 and 0.53 Torr, Penning ionization is almost completely responsible for the Cu-atom ionization (i.e., 86% and 91% at 2 and 1 mA, respectively). With increasing pressure, at constant current, the opposite tendency is observed. As the pressure rises, the density of the Ar^+ ions and electrons increases, while the Ar^m density decreases. Moreover, due to the higher electron density, the loss of metastable atoms by thermal-electron quenching becomes more important at higher pressures and currents. Hence, at higher pressures and currents, the radial profiles of the Ar^m change, compared with the profiles at low pressures. Indeed, the Ar^m density then shows a minimum at the position where the slow-electron density has a maximum, i.e., at the discharge axis. Therefore, the relative importance of Ar^+ ion ACT in the NG increases. However, integrated over the entire HCD volume, Penning ionization is still the main production mechanism of Cu^+ ions. For example, for a discharge at 1 Torr and 9 mA, the relative contribution of Penning ionization, ACT, and electron-impact ionization amount to 68%, 26%, and 6%, respectively.

E. Density of the Cu^+ ions

The ion population is the result of both the density and the ionization efficiency of the sputtered atoms. Figures 9

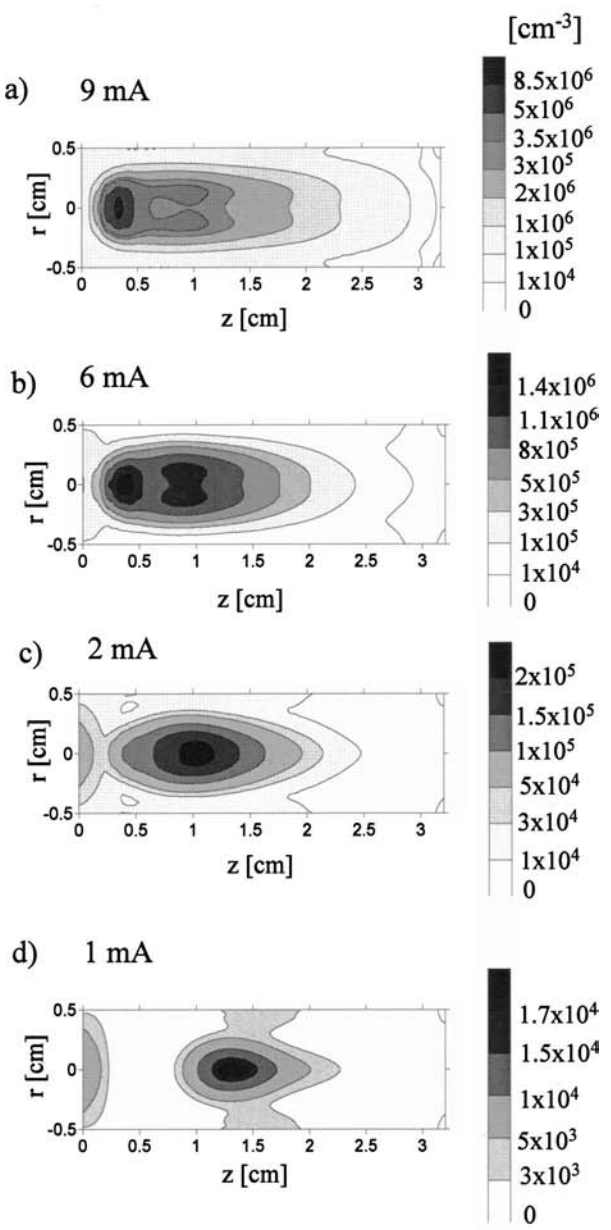

FIG. 9. Calculated two-dimensional profiles of the Cu^+ ion density at 0.3 Torr and four different currents: 9 (a), 6 (b), 2 (c), and 1 mA (d).

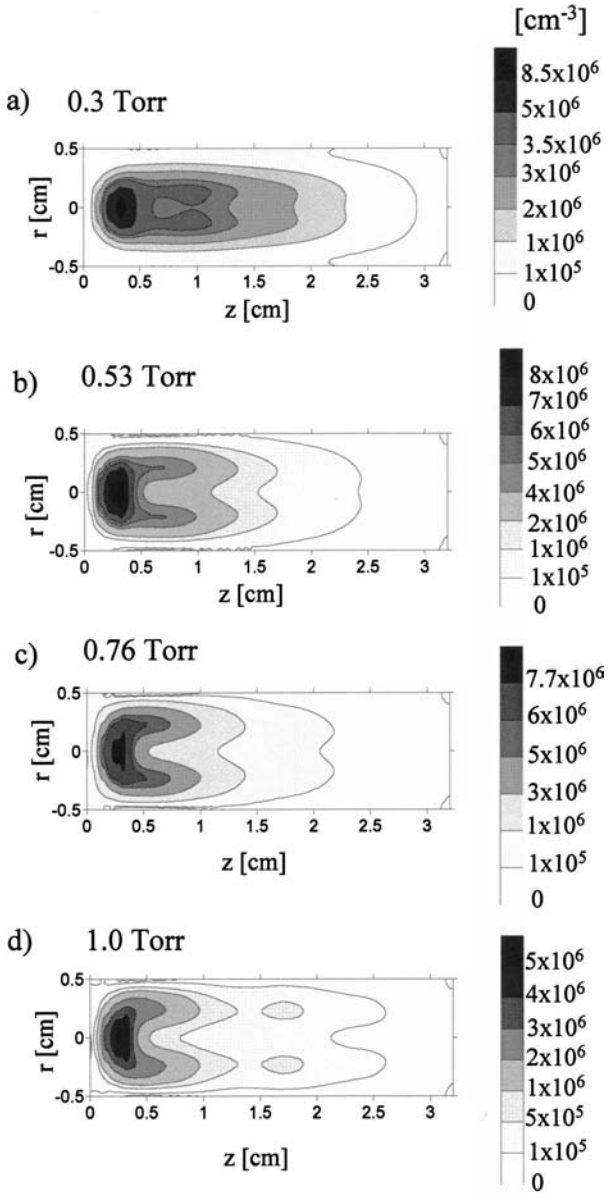

FIG. 10. Calculated two-dimensional profiles of the Cu^+ ion density at 9 mA and four different pressures: 0.3 (a), 0.53 (b), 0.76 (c), and 1.0 Torr (d).

and 10 illustrate the two-dimensional Cu^+ ion density profiles at 0.3 Torr and four different currents and at 9 mA and four different pressures, respectively. Compared to the Cu-atom spatial distribution, the Cu^+ ion population is more shifted in the radial direction toward the axis, because the ionization is mainly caused by Penning ionization and ACT (see above) and the densities of the Ar^m and Ar^+ ions are low near the cathode wall. At 0.3 Torr and 9 mA the Cu^+ ion density profile peaks at the cylinder axis in the lower half of the cylinder. Further away from the cathode bottom, the Cu^+ ion density profile shows a small dip at the cylinder axis and two small maxima at both sides off axis (donut shape), as can be observed in Fig. 9(a). With decreasing current, the Cu^+ ion density drops drastically close to the bottom cathode and the two small peaks off axis begin to merge (i.e., the donut closes in the middle). At low currents, the maximum population is found at the center of the discharge [Fig. 9(d)].

With increasing pressure (see Fig. 10), the Cu^+ ion population decreases and becomes concentrated almost completely in the lower half of the cylinder. In the radial direction, the density profiles do not change very much, i.e., they exhibit two peaks at high currents (see Fig. 9) and a common peak at the cylinder axis, at low currents.

The ionization degree of the Cu atoms was found to be around 10^{-5} for all conditions investigated. In the case of Ar atoms, the ionization degree was in the same order. Therefore, the relation of the Cu^+ ion population to the Ar^+ ion population is similar to the ratio of the Cu atom to Ar atom population and is in the order of 10^{-4}.

IV. CONCLUSIONS

We have developed a model to describe the behavior of the sputtered Cu atoms and Cu^+ ions in a HCD. It was found

that the energetic Ar^+ ions play the most important role for the sputtering of the cathode. The role of self-sputtering was negligible, in contrast to planar GDs, where the contribution of self-sputtering was typically in the order of several percentages.[52] At the cathode bottom, there is no net sputtered flux, but there is a net amount of redeposition, while at the cathode sidewalls, redeposition predominates only close to the cathode bottom and near the open end towards the anode. Throughout the discharge volume, at all the conditions investigated, the largest concentration of Cu atoms was found in the lower half of the HCD, close to the bottom, at some distance from the cathode surface (both at the cathode bottom and at the cathode sidewalls). At low pressures, the Cu-atom population is more uniformly distributed along the discharge length, and the density profiles show a maximum at the cylinder axis, close to the cathode bottom, while at higher pressures, the maximum was found close to the cathode sidewalls. Moreover at 1 Torr, regions of high Cu-atom density alternate with a region of low density, which corresponds to the formation of the characteristic consecutive hollow spheres observed experimentally in HCDs. Penning ionization was found the main ionization mechanism for the Cu atoms, followed by Ar^+ ion ACT. The ionization degree of the Cu atoms was found to be in the order of 10^{-5} for all conditions investigated.

ACKNOWLEDGMENTS

This research is sponsored by the Flemish Fund for Scientific Research, by NATO's Scientific Affairs Division in the framework of the Science for Peace Programme and by the Federal Services for Scientific, Cultural and Technical Affairs of the Prime Minister's Office through IUAP V. The authors also acknowledge R. Gijbels for his interest in this work.

[1] G. K. Wehner, Phys. Rev. **102**, 690 (1956).
[2] B. Chapman, *Glow Discharge Processes: Sputtering and Plasma Etching* (Wiley, New York, 1980).
[3] I. G. Ivanov, E. L. Latush, and M. F. Sem, *Metal Vapour Ion Lasers: Kinetic Processes and Gas Discharges* (Wiley, Chichester, 1996).
[4] N. K. Vuchkov, K. A. Temelkov, and N. V. Sabotinov, IEEE J. Quantum Electron. **35**, 1799 (1999).
[5] P. J. Slevin and W. W. Harrison, Appl. Spectrosc. Rev. **10**, 201 (1975).
[6] S. Caroli, Prog. Anal. At. Spectrosc. **6**, 253 (1983).
[7] C. Yang and W. W. Harrison, Spectrochim. Acta, Part B **56**, 1195 (2001).
[8] D. M. Manos and D. L. Flamm, *An Introduction to Plasma Etching* (Academic, New York, 1989).
[9] A. Goldamn and J. Amoroux, *Gases: Macroscopic Processes and Discharges* (Plenum, New York, 1983).
[10] H. Helm, Z. Naturforsch. A **27A**, 1812 (1972).
[11] V. I. Kolobov and L. D. Tsendin, Plasma Sources Sci. Technol. **4**, 551 (1995).
[12] C. Yang and W. W. Harrison, Spectrochim. Acta, Part B **56**, 1195 (2001).
[13] E. H. Daughtrey, D. L. Donohue, P. J. Slevin, and W. W. Harrison, Anal. Chem. **47**, 683 (1975).
[14] R. M. Allot, M. Kubinyl, A. Grofcsik, W. J. Jones, and R. S. Mason, J. Chem. Soc., Faraday Trans. 9, 1297 (1995).
[15] D. R. Oliver and T. R. Finlayson, J. Anal. At. Spectrom. **13**, 443 (1998).
[16] G. Gergelyi and Z. Szilvassy, ACH-Models Chem. **136**, 69 (1999).
[17] W. Hang and W. W. Harrison, Anal. Chem. **69**, 4957 (1997).
[18] B. E. Warner and K. B. Persson, J. Appl. Phys. **50**, 5694 (1979).
[19] E. M. van Veldhuizen and F. J. Hoog, J. Phys. D **17**, 953 (1984).
[20] S. C. Rae and R. C. Tobin, J. Appl. Phys. **64**, 1418 (1988).
[21] A. J. Lichtenberg and M. A. Lieberman, J. Appl. Phys. **87**, 8191 (2000).
[22] D. R. Oliver and T. R. Finlayson, J. Phys. D **31**, 1857 (1998).
[23] J. A. Valles Abarca and A. Gras-Marti, J. Appl. Phys. **55**, 1370 (1984).
[24] R. R. Arslanbekov, R. C. Tobin, and A. A. Kudryatsev, J. Phys. D **81**, 554 (1997).
[25] G. J. Fetzer and J. J. Rocca, IEEE J. Quantum Electron. **28**, 1941 (1992).
[26] A. Tran Ngoc, E. Marode, and P. C. Johnson, J. Phys. D **10**, 2317 (1977).
[27] A. Bogaerts, M. van Straaten, and R. Gijbels, Spectrochim. Acta, Part B **50**, 179 (1995).
[28] J. P. Boeuf, J. Appl. Phys. **63**, 1342 (1988).
[29] D. Paschier and W. J. Goedheer, J. Appl. Phys. **74**, 3744 (1993).
[30] G. Bano, L. Szalai, P. Horvath, K. Kutasi, Z. Donko, K. Rozsa, and T. M. Adamowiccz, J. Appl. Phys. **92**, 6372 (2002).
[31] A. Bogaerts and R. Gijbels, J. Appl. Phys. **92**, 6408 (2002).
[32] R. R. Arslanbekov, A. A. Kudryatsev, and R. C. Tobin, Plasma Sources Sci. Technol. **7**, 310 (1998).
[33] N. Baguer, A. Bogaerts, and R. Gijbels, J. Appl. Phys. **94**, 2212 (2003).
[34] M. Surendra, D. B. Graves, and G. M. Jellum, Phys. Rev. A **41**, 1112 (1990).
[35] A. Bogaerts and R. Gijbels, Phys. Rev. A **52**, 3743 (1995).
[36] K. Tachibana, Phys. Rev. A **34**, 1007 (1986).
[37] N. Baguer, A. Bogaerts, Z. Donko, R. Gijbels, and N. Sadeghi, J. Appl. Phys. **97**, 123305 (2005).
[38] N. Baguer, A. Bogaerts, and R. Gijbels, Spectrochim. Acta, Part B **57**, 311 (2002).
[39] N. Matsunami *et al.*, At. Data Nucl. Data Tables **31**, 1 (1984).
[40] P. Sigmund, *Topics in Applied Physics* (Springer, Berlin, 1984).
[41] J. Linhard, M. Scharff, and H. E. Schiott, Mat. Fys. Medd. K. Dan. Vidensk. Selsk. **33**, 14 (1963).
[42] J. Sielanko, Radiat. Eff. Lett. Sect. **86**, 185 (1984).
[43] T. C. Bradbury, *Mathematical Methods with Applications to Problems in the Physical Sciences* (Wiley, New York, 1984).
[44] A. Bogaerts and R. Gijbels, J. Appl. Phys. **79**, 1279 (1996).
[45] D. U. Rosenberg, *Methods for the Numerical Solutions of Partial Differential Equations* (Elsevier, New York, 1969).
[46] A. Bogaerts, E. Wagner, B. W. Smith, J. D. Winefordner, D. Pollmann, W. W. Harrison, and R. Gijbels, Spectrochim. Acta, Part B **52**, 205 (1997).
[47] R. V. Stuart and G. K. Wehner, J. Appl. Phys. **33**, 2345 (1962).
[48] W. Hang and W. W. Harrison, Anal. Chem. **69**, 4957 (1997).
[49] M. van Straaten, A. Bogaerts, and R. Gijbels, Spectrochim. Acta, Part B **50**, 583 (1995).
[50] R. V. Stuart and G. K. Wehner, J. Appl. Phys. **35**, 1819 (1964).
[51] J. Hamish and J. de la Rosa, Appl. Phys. B **43**, 189 (1987).
[52] A. Bogaerts and R. Gijbels, Anal. Chem. **68**, 2676 (1996).